A&A, 706, A207 (2026)
https://doi.org/10.1051/0004-6361/202557757

Astronomy & Astrophysics

Selection and characterisation of the M dwarf targets in the PLATO Input Catalogue

L. Prisinzano[1,⋆], M. Montalto[2], G. Piotto[3,4], P. M. Marrese[5,6], S. Marinoni[5,6], V. Nascimbeni[4,7], V. Granata[7,4], J. Cabrera[8], K. Belkacem[9], M. Deleuil[10], L. Gizon[11], M. J. Goupil[9], I. Pagano[2], D. Pollacco[12], R. Ragazzoni[3,4], H. Rauer[8,13], S. Udry[14], J. Maldonado[1], G. Micela[1], F. Damiani[1], L. Affer[1], G. Altavilla[5,6], C. Argiroffi[15,1], S. Benatti[1], S. Cassisi[16], R. Claudi[4,17], S. Desidera[4], M. Fabrizio[5,6], E. Flaccomio[1], U. Heiter[18], A. F. Lanza[2], A. Maggio[1], L. Malavolta[3,4], D. Nardiello[3,4], S. Ortolani[3,4], and A. Sozzetti[19]

(Affiliations can be found after the references)

Received 20 October 2025 / Accepted 10 December 2025

ABSTRACT

Context. The aim of the European Space Agency's PLAnetary Transits and Oscillations of Stars (PLATO) mission is to detect planets orbiting around dwarfs and subgiant stars with spectral type F5 or later, including M dwarfs. The PLATO Input Catalogue (PIC) contains all PLATO targets available for observation by the PLATO nominal science. The latest version, PIC 2.1.0.1, focuses on the Southern PLATO field, named LOPS2, selected as the first long observation field, and includes the P4 sample, one of the four target samples outlined in the Science Requirement Document. P4 includes the M dwarfs with magnitudes brighter than V=16 located within LOPS2.

Aims. A characterisation of the M dwarfs in the PIC is essential for assessing their potentiality to host exoplanets, and eventually for estimating the hosted planet(s) properties. The purpose of this paper is to describe how we selected the P4 M dwarf targets, and obtained their fundamental parameters and properties.

Methods. Measuring stellar parameters is a challenging task. Interferometry provides direct estimates of radii, whereas alternative approaches relying on theoretical assumptions are still affected by significant uncertainties. In this work, we introduce the P4 sample and detail the methodologies, all based on photometric criteria, adopted for the measurement of their stellar parameters.

Results. Based on a statistical analysis of the P4 sample, we assess both the photometric and volume completeness, and classify the stellar populations according to their Galactic spatial-velocity components. The adopted stellar parameters are validated by comparison with independent methods from the literature used to estimate stellar radii.

Conclusions. We conclude that the P4 sample is compliant with the PLATO science requirements. Being magnitude limited, its volume completeness decreases going towards distances larger than 30 pc, where late-type targets are progressively less covered. The observed large spread in the colour-magnitude diagram is likely due to the combination of several effects such as metallicity, age, binarity, and activity. The strategy we adopted for deriving stellar parameters provides results consistent with those obtained in the literature with different and independent methods.

Key words. techniques: photometric – catalogs – planets and satellites: terrestrial planets – stars: fundamental parameters – stars: late-type – stars: low-mass

1. Introduction

The PLAnetary Transits and Oscillations of Stars (PLATO) mission (Rauer et al. 2014, 2025) is an M-class mission of the European Space Agency (ESA). It is scheduled to be launched in late 2026, and its primary aim is to search for and characterise terrestrial exoplanets orbiting stars similar to our Sun by employing the transit method. The PLATO mission will generate two primary types of data: light curves and imagettes; however, due to telemetry limitations, only the data of pre-selected targets will be downloaded and analysed. The PLATO target samples will be located in the Long-duration Observation Phase (LOP) PLATO fields (Nascimbeni et al. 2022, 2025), and are presently available to all PLATO consortium members through the PLATO Input Catalogue (PIC). A version of the PIC will become public nine months before the PLATO launch. We refer to Montalto et al. (2021) for a complete description of the PLATO samples.

PLATO's primary mission objectives focus on observing F, G, and K spectral type stars, including Sun analogues. The targets are formally grouped into four samples (Montalto et al. 2021), in agreement with the ESA PLATO Science Requirements (Rauer et al. 2025). One of these is the P4 sample, which contains the cool late-type dwarf targets that are the focus of this paper.

The M-type main-sequence stars selected for the P4 sample are of great interest in the field of extrasolar planets for several reasons. The stellar initial mass function (IMF) peaks between 0.1 and 0.5 $M_\odot$, making M-type stars the most common stars, with a single star fraction reaching values of ∼75% (Lada 2006). In addition, M-type stars have a better star/planet luminosity contrast with respect to solar-type stars. Considering a planet with fixed mass and orbital properties, the stellar radial velocity semi-amplitude due to the presence of a planet is a factor $\gtrsim$2 larger for M dwarfs than for solar-type stars. From the photometric point of view, the transit depth scales with the square of the

⋆ Corresponding author: loredana.prisinzano@inaf.it

ratio of the planetary to stellar radii $R_P/R_\star$. This means that, for a fixed planetary size, smaller host stars produce deeper transits, making them significantly easier to detect (Nascimbeni et al. 2012; Lovis et al. 2017). Finally, the habitable zone (HZ) is closer (within 0.1–0.2 AU) to the host star (Kopparapu et al. 2013), and this increases the probability of detecting transiting planets in HZ by a factor of 2–3, as well as the transit frequency during observations. This makes such a sample particularly important for statistically probing the inner edge of the HZ, including the hypothesised HZ inner edge discontinuity, as demonstrated in simulations computed for PLATO (Schlecker et al. 2024).

Planet formation around M dwarfs is fundamentally challenged by their low-mass protoplanetary disks, which contain insufficient material for traditional core accretion to build gas giant cores before the gas dissipates. The leading solution is the pebble accretion model, where a growing core can efficiently sweep up pebble-sized particles, rapidly assembling the mass needed to form the super-Earths and mini-Neptunes commonly observed around these stars (Lambrechts & Johansen 2012). The alternative disk instability model is considered unviable as M dwarf disks lack the requisite mass to become gravitationally unstable (Kratter & Lodato 2016). Consequently, the observed rarity of gas giants and abundance of smaller planets around M dwarfs serves as a crucial observational test, strongly favouring pebble accretion as the dominant formation mechanism in low-mass stellar systems (Dressing & Charbonneau 2015).

M dwarfs are intrinsically faint in the optical bands, and mostly emit in the near-infrared (NIR). Moreover, they are strongly affected by magnetic activity (Kochukhov 2021) and their spectra are dominated by molecular bands, which complicates their characterisation, particularly the precise determination of stellar parameters and chemical abundances (Maldonado et al. 2015, 2020; Olander et al. 2025). Determining stellar radii is especially challenging due to their intrinsically small sizes, and only a limited number of direct radius measurements obtained through long-baseline interferometry are available (Boyajian et al. 2012). Direct radii can be also obtained from SB2 eclipsing binaries (EBs) using dedicated NIR spectroscopy (Maxted et al. 2022). Nonetheless, a significant advantage is that M dwarfs are the most numerous stellar type in the Galaxy and, due to their high local spatial density, a large number of them are found in the solar neighbourhood. This makes them an ideal population for statistical studies and for testing stellar structure and evolution models through comparisons with direct measurements (Cassisi & Salaris 2019).

As first found by Berger et al. (2006), interferometrically derived radii are 15–20% larger than those predicted by theoretical models based on bolometric luminosity. Such a discrepancy, also known as the radius inflation problem, has also been found for detached double-lined EBs for which precise and accurate measurements of stellar masses and radii have been determined (e.g. Torres 2007; Irwin et al. 2011). More recent interferometric and *Gaia*-based studies of single, slowly rotating, magnetically inactive M dwarfs indicate that radius inflation in single stars is generally less pronounced, typically in the 0–7% range, compared to 5–20% in eclipsing binaries (e.g. Kesseli et al. 2018; Morrell & Naylor 2019; Wanderley et al. 2024; Kiman et al. 2024). This suggests that while binarity and rapid rotation play a significant role, other mechanisms such as magnetic activity, starspots, metallicity, and stellar age may also contribute. Berger et al. (2006) found some evidence that the reported discrepancies correlate with metallicity, increasing with higher metal content. They interpreted this effect as evidence of shortcomings in the current generation of opacity tabulations used in stellar modelling. Nevertheless, the presence of magnetic activity and, in particular, correlated starspots, has long been considered (Spruit 1982; Spruit & Weiss 1986; MacDonald & Mullan 2012; Cassisi & Salaris 2013; Feiden & Chaboyer 2013, 2014) the most plausible explanation for the radius inflation problem. Starspots reduce the effective radiating surface area of a star, leading to the radius inflation. A treatment of the effects of starspots at the photospheric level on the stellar evolution models by Tognelli et al. (2018) is presented in Franciosini et al. (2022) and show that other stellar parameters, such as effective temperatures, are also affected by the presence of starspots.

Swayne et al. (2024) measured the masses, radii, and effective temperatures of 23 M dwarf companions to solar-type stars using CHEOPS observations. Using high-precision light curves from CHEOPS and comparing them with TESS data, for most targets they found evidence of radius inflation. The authors accounted for starspot-induced variations in their measurements and found trends linking radius inflation to metallicity.

Recent studies have shown that single magnetically inactive M dwarfs exhibit smaller or negligible radius inflation, while active single stars can still display significant inflation, particularly at masses around 0.5–0.6 $M_\odot$, exactly the stellar mass range targeted by PLATO. At lower masses the effect appears less pronounced, which may reflect either larger measurement uncertainties or intrinsic physical differences in the stellar interior structure (e.g. Kesseli et al. 2018; Wanderley et al. 2024; Kiman et al. 2024).

In this work we present the selection and characterisation of the P4 sample included in the PIC 2.1.0.1 located within the first LOP (LOPS2, Nascimbeni et al. 2025) footprint in order to give a general astrophysical description of the sample. The methods adopted for the sample selection and the parameter derivation are described in Sect. 2. The results, including the photometric and volume completeness of the sample and the analysis of the kinematics are presented in Sect. 3. A comparison of the stellar radii with those from other studies and a discussion of the possible effects of the observed spread in the *Gaia* colour-absolute magnitude diagram are presented in Sect. 4, while our conclusions are given in Sect. 5.

2. Methods

2.1. Data

The main reference catalogue for the selection of the targets of the most recent version of the PIC, including the P4 sample, is *Gaia* DR3 (Gaia Collaboration 2016, 2023b). As for the distances, we adopted the values provided by Bailer-Jones et al. (2021). In addition, to derive the stellar parameters of the P4 sample, we also used 2MASS data (Skrutskie et al. 2006).

The main strategy adopted to select the targets for the Plato samples, including the P4 sample is described in Montalto et al. (2021), in which an all-sky version of the PIC (asPIC 1.1.0), based on *Gaia* DR2 data, has been presented.

A new version of the PIC, named PIC 2.1.0.1, has been released to the PLATO Consortium on 21 February 2025. This version is limited to the LOPS2 footprint (Nascimbeni et al. 2025, LOPS2) and is based on *Gaia* DR3. It also includes additional subPICs: fine guidance stars (fgPIC), instrument calibration targets (cPIC), and stellar astrophysics calibration targets (scvPIC). This paper is based on the PIC 2.1.0.1.

Table 1. Best-fit coefficients of the $(G-V)_0$ vs $(G_{BP}-G_{RP})_0$ relation for dwarf stars. Validity range: $-0.51 \leq (G_{BP}-G_{RP})_0 \leq 5.75$.

b_1	b_2	b_3	b_4	b_5	b_6	σ
−0.0085337	−0.2422638	0.0493499	−0.0161423	0.0038450	−0.0003356	0.017

2.2. Stellar sample selection

The PLATO science requirements impose the following conditions:

- the total number of cool late-type dwarfs in stellar sample 4, P4, (cumulative over all sky fields observed by PLATO) shall be at least 5000, to be monitored during a Long-Duration Observation Phase;
- the dynamic range of stellar P4 shall be $m_V \lesssim 16$;
- it shall be possible to obtain imagettes of 5000 targets in stellar sample 4 with a sampling time equal to 25 seconds.

Since the selection must be based on the visual V magnitude, this quantity was included in the PIC for each target. The visible magnitude was set equal to the Johnson V magnitude when available in the literature; otherwise, it was estimated. Since literature available photometric conversions do not cover the low-mass M-type regime, we derived a photometric calibration providing a new conversion from the *Gaia* DR3 photometric system to the Johnson-Cousins system. The calibration relation that we derived from a least-squares best-fit procedure is a sixth-order polynomial of the form

$$(G-V)_0 = \sum_{i=1}^{i=6} b_i (G_{BP}-G_{RP})_0^i, \quad (1)$$

where the colours are those of dwarf star models taken from the MPSA, MARCS, POLLUX/AMBRE, POLLUX/BT-Dusty, POLLUX/CMFGEN, and COELHO stellar libraries. The relation is valid in the range $-0.51 \leq (G_{BP}-G_{RP})_0 \leq 5.75$. The best-fit coefficients are listed in Table 1, and the corresponding relation is illustrated in Fig. 1, showing the result, the adopted colours and the residuals of the fit.

Given the very small uncertainties in the *Gaia* DR3 $(G_{BP}-G_{RP})_0$ colours for stars within the considered magnitude range, the low expected extinction, and the limited effect of the sixth-order polynomial (at most a few hundredths of a magnitude), the choice of a sixth-order fit does not impact the selection of the P4 sample.

The selection of the P4 sample targets has been performed by assuming the spectral type calibration given in Pecaut & Mamajek (2013) in which the spectral type M0 corresponds to $T_{eff} = 3850$ K. To define the magnitude and colour boundaries for the selection in the colour-absolute magnitude diagram (CAMD), we adopted the Galactic simulations TRILEGALv1.6 (Girardi et al. 2005) falling in the region of the LOPS2 field.

In order to define the blue selection boundary, we considered two representative samples. The first one includes the targets, defined as stars having $T_{eff} < 3850$ K and $\log g > 3.5$ and $V \leq 16$, as obtained from the Galactic simulations. These correspond to M dwarfs. The second sample includes the contaminants, defined as all stars with $V \leq 16$ that do not meet the target criteria, i.e. stars with $T_{eff} > 3850$ K and/or $\log g < 3.5$. In this context, the contaminants are mainly FGK dwarfs. For the blue boundary, the goal is to separate M dwarfs (the P4 targets) from FGK dwarfs (the contaminants) in the colour–magnitude diagram. The best separation colour boundary was defined as the line around the blue limit of the targets, maximising the metric $S = (N_{targ} - N_{cont})$, where N_{targ} and N_{cont} are respectively the number of targets and contaminants. The final separation boundary in this case corresponds to the theoretical best separation boundary and is given by the equation $M_{G,0} = -8.62(G_{BP}-G_{RP})_0 + 24.96$, where $M_{G,0}$ is absolute magnitude in the *Gaia* G band, corrected for absorption and $(G_{BP}-G_{RP})_0$ are the reddening corrected *Gaia* colours. Absorption and reddening were derived using the Lallement et al. (2018) dust map, as described in Montalto et al. (2021).

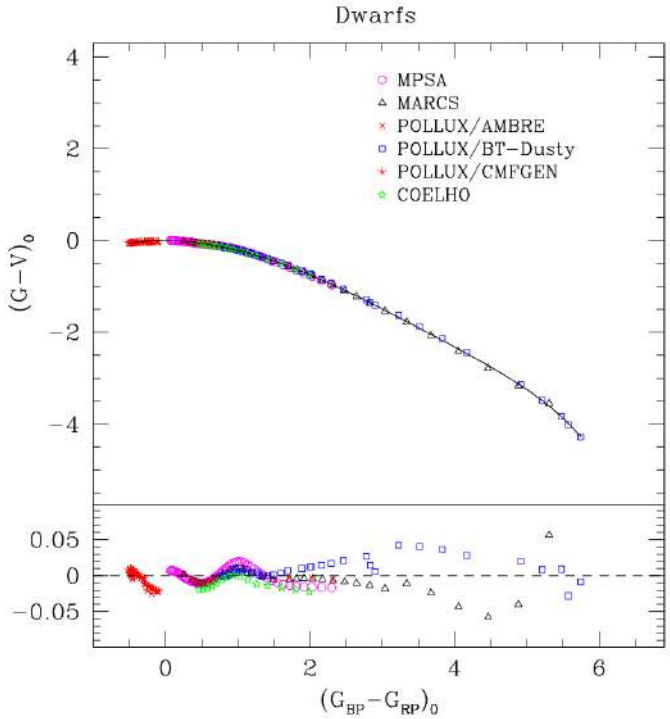

Fig. 1. *Top*: synthetic two-colour diagram of $(G-V)_0$ vs $(G_{BP}-G_{RP})_0$ for dwarf star models taken from the stellar libraries indicated in the legend. The solid line represents the best-fit polynomial to the synthetic colours. *Bottom*: residuals between the synthetic $(G-V)_0$ values and the best-fit relation, plotted as a function of the synthetic $(G_{BP}-G_{RP})_0$ colour.

As for the PIC 1.1.0, the boundary at the bright and red side of the M dwarf selection region corresponds to the best regression line of a 10 Myr solar metallicity isochrone from the PARSEC database (Bressan et al. 2012). The separation boundary is given by the following equation: $M_{G,0} = 2.334(G_{BP}-G_{RP})_0 + 2.259$.

In conclusion, the selection criteria adopted for the P4 sample are

$$\begin{cases} M_{G,0} \geq 2.334(G_{BP}-G_{RP})_0 + 2.259 \\ M_{G,0} > -8.62(G_{BP}-G_{RP})_0 + 24.96. \\ V \leq 16. \end{cases} \quad (2)$$

With these conditions we selected 15140 targets suitable for the P4 sample. Figure 2 shows the CAMD of the selected targets.

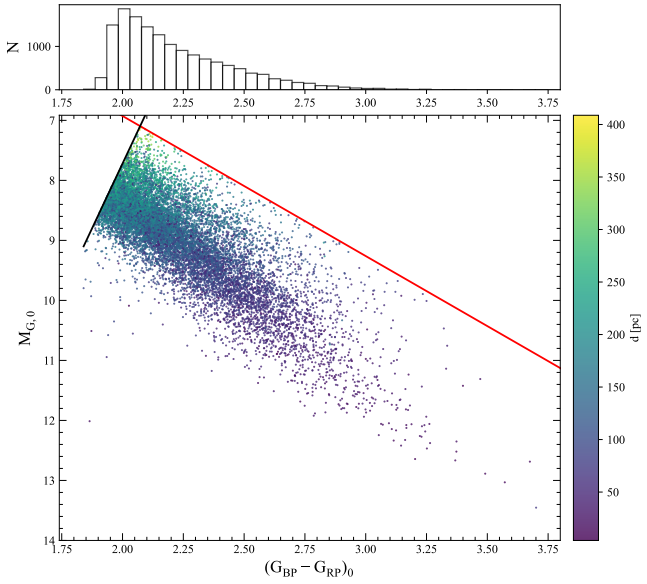

Fig. 2. Colour–absolute magnitude diagram of the P4 sample targets. The colour map indicates the distance of the targets. The black and red lines represent the adopted limits indicated by the first two relations given in Eq. (2). The histogram of the $(G_{BP} - G_{RP})_0$ colours is also shown in the top panel.

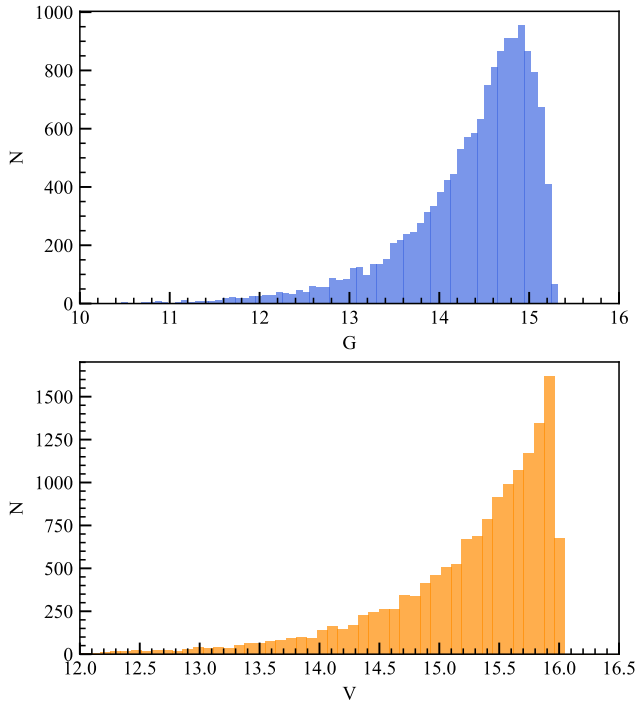

Fig. 3. Distribution of apparent G and V magnitudes for the P4 sample.

The figure illustrates also the distances of the targets of the P4 sample, and the histogram shows how the number of targets decreases towards later spectral types, which are intrinsically fainter and therefore detected only at shorter distances.

The M dwarf sample consists of 15157 targets obtained adding to the P4 sample, defined above, 17 additional M dwarfs which satisfy the first two conditions in Eq. (2), but have V>16. The additional targets are M dwarfs with confirmed and/or candidate planets retrieved from the catalogue Exo-MerCat (Alei et al. 2020, 2025).

The mean distance of the P4 sample targets, computed from the distances provided by Bailer-Jones et al. (2021), is 135.4 pc, while the median distance is 133.0 pc. The standard deviation is σ_d = 59.3 pc, while the minimum and maximum distances observed in the sample are $d_{\rm min}$ = 3.9 pc, corresponding to the Kapteyn's star, and d_{max} = 408.8 pc, respectively. The magnitude distributions in both the G and V bands are shown in Fig. 3.

2.3. Validation of P4 targets and K_S magnitudes

To derive stellar radii and masses for the P4 sample targets, we need the absolute K_S magnitudes (see Sect. 2.4.2) from the 2MASS catalogue (Skrutskie et al. 2006). The 2MASS near infrared colours can also be used to validate the P4 sample, since, based on the stellar evolution model predictions, M-type stars are expected to have $J - H$, $H - K_S$, and $J - K_S$ colours in well defined ranges (e.g. Bressan et al. 2012). For this purpose, the P4 sample was cross-matched with 2MASS using the official *Gaia*-2MASS cross-match procedure (Marrese et al. 2019), ensuring completeness by systematically identifying the best 2MASS counterparts for all *Gaia* stars.

To validate the cross-match and ensure the reliability of the K_S magnitudes for stellar parameter derivation, we considered only one-to-one matches between *Gaia* and 2MASS. In addition, in cases where multiple *Gaia* sources (mates, Marrese et al. 2019) shared the same best 2MASS match, only those mates classified as M-type stars were retained. All matched stars were compiled into a single list, resulting in a total of 14 909 objects from the original Mdwarf sample including 15 157 stars.

We note that no M-type stars with a 2MASS counterpart has more than one neighbour.

Figure 4 displays the near infrared colour–colour diagram of the targets included in the P4 sample. The majority of the sources lie within the colour space typically occupied by M-type stars, indicated by the cyan curve representing the colours of stars between M0V and M6V (Pecaut & Mamajek 2013), confirming the consistency of their photometric properties with this classification. However, a significant spread is evident, which may arise from a combination of photometric uncertainties, unresolved binarity, stellar activity (e.g. spots), and possibly metallicity variations. In order to identify the few outliers that are not compatible with M-type stars or for which the 2MASS photometry is not reliable for parameter derivation, we performed a statistical analysis of the $J - H$, $H - K_S$, and $J - K_S$ colour distributions, using the boxplots, shown in Fig. 5. In particular, we considered the interquartile range (IQR) i.e. IQR =Q3–Q1, where Q3 = 75th percentile and Q1 = 25th percentile. The median (red line), the IQR (black box), and the full spread of the distributions are shown in each panel. Table 2 reports the main statistical parameters for each colour index, including the median, Median Absolute Distribution (MAD), quartiles, and the corresponding thresholds for outlier identification.

The thresholds used to identify the blue outliers, i.e. objects with the most reliable 2MASS photometry in the three bands[1], that are not consistent with M-type stars, have been defined by considering the lower tails of these distributions, corresponding to the boundaries beyond which sources deviate significantly from the bulk of the M dwarf population. In particular, for each of the three $J - H$, $H - K_S$, and $J - K_S$ colours, we considered the IQR and we defined the Outer fence range as [Q1–3×IQR,

[1] ph_qual=AAA in the JHKs bands.

Table 2. Statistical properties of the 2MASS colour indices in the P4 sample.

Colour	Median	MAD	Q1	Q3	Q1 – 3 × IQR	Q3 + 3 × IQR	Min	Max
$J-H$	0.62	0.03	0.59	0.65	0.41	0.83	–1.50	1.99
$H-K_S$	0.22	0.02	0.20	0.24	0.08	0.32	–1.22	1.53
$J-K_S$	0.84	0.03	0.82	0.87	0.67	1.01	–1.27	2.26

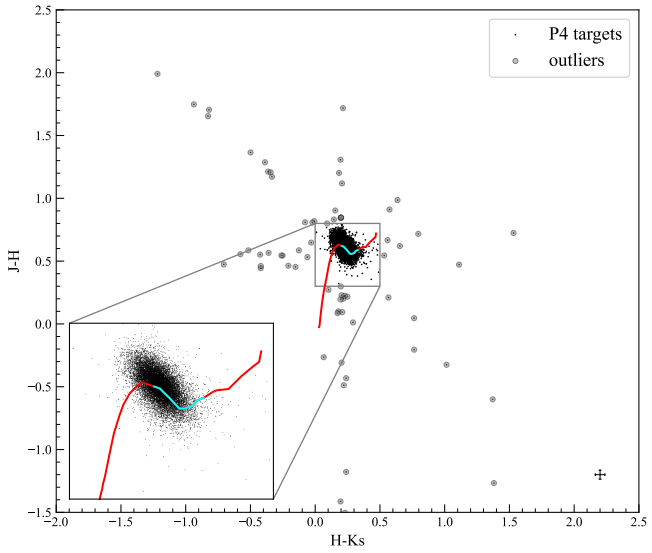

Fig. 4. Near-infrared (J–H vs H–Ks) colour–colour diagram of the P4 sample targets. The grey circles highlight the outliers in this diagram. The solid red line shows the mean colours of dwarfs from Pecaut & Mamajek (2013). The cyan line indicates the subset of stars from M0V to M6V. The inset provides a zoomed-in view of the high-density core of the distribution, allowing better visualisation of the main-sequence locus. The typical errors in the colours are indicated in the bottom right corner.

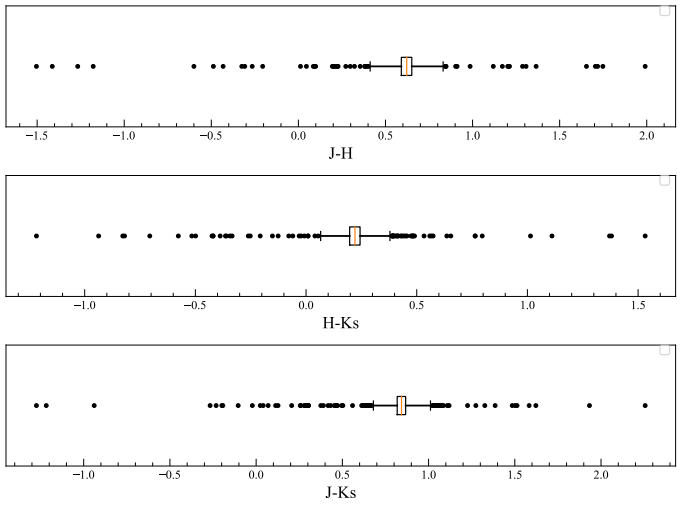

Fig. 5. Boxplots of the $J-H$, $H-K_S$, and $J-K_S$ colour distributions for the selected P4 sample. Each box represents the IQR (25th to 75th percentile), with the central red line indicating the median. The whiskers extend to the most extreme data points that are not considered outliers. The individual points beyond the whiskers represent outliers, i.e. values that deviate significantly from the main distribution.

Q3+3×IQR]. We found that the colour dispersion evaluated with the MAD is very similar to the IQR, since most of the data are concentrated around a narrow colour range.

We defined blue outliers, objects with good 2MASS photometry, for which one of the three 2MASS colours is smaller than the lower outer fence values Q1–3×IQR, corresponding to –4.72σ (assuming that Q1 and Q3 lies at –0.675σ and at 0.675σ in a gaussian distribution). The criteria to select these blue outliers are, therefore, $J-H < 0.41$ or $H-K_S < 0.06$ or $J-K_S < 0.67$.

Analogously, we defined red outliers, objects for which one of the three 2MASS colours is larger than the upper outer fence values Q3+3×IQR, corresponding to 4.72σ. The criteria used to select these red outliers are therefore $J-H > 0.83$, $H-K_S > 0.39$, or $J-K_S > 1.01$.

In conclusion, from the P4 sample included in the matched list, we discarded eight stars with 2MASS ph_qual=AAA, classified as blue outliers. We note that additionally three more objects with $G_{BP}-G_{RP} < 1.84$ were excluded as their colours are not consistent with those of M dwarfs. In addition, we identified 53 red outliers that were retained in the P4 sample as M-type targets, but for which stellar parameters were not derived as their 2MASS colours are redder than expected for single main-sequence M-type stars, and are likely not representative of the stellar photosphere.

Based on these considerations and the analysis of the 2MASS quality flags, the P4 targets cross-matched with 2MASS (one-to-one matches) that were validated and for which stellar parameters can be derived with the 2MASS Ks magnitude, are 14328 out of 14909 (96%). In addition, we found 320 stars (about 2% of the total sample) with one mate (a neighbour star) for which the 2MASS photometry is consistent with that expected for M-type stars. These 14 648 (14 328+320) objects can be considered valid for the P4 sample as their NIR colour-colour diagrams are compliant with those expected for M-type stars. Stellar parameters for these targets have been derived with the 2MASS Ks magnitude.

For the remaining 261 (14 909–14 648) targets, we concluded that while they can be considered valid for the P4 sample, the 2MASS Ks magnitudes are not reliable for the stellar parameter derivation.

2.4. Stellar parameters

2.4.1. Effective temperatures

In the absence of complete sets of spectroscopic data (*Gaia* DR3 Radial Velocity Spectrometer going down to $G \lesssim 14$), homogeneous and consistent effective temperatures for photometrically selected samples, such as those selected for the PIC, can only be derived through the adoption of a photometric calibration. To this aim, we adopted a set of FGK dwarfs from the dataset of Casagrande et al. (2010) and a set of M dwarfs from the dataset of Mann et al. (2015). The FGK dwarfs were cross-matched with

Table 3. Best-fit coefficients of the $T_{\rm eff}$ as a function of $(G_{\rm BP} - G_{\rm RP})_0$ relationship represented by Eq. (3).

c_0	c_1	c_2	c_3	c_4	c_5	σ
9649.1817	–7175.80969	3642.30312	–1020.37499	146.20008	–8.30455	55 K

Gaia DR3, selecting only stars within 70 pc that met our quality criteria, yielding a sample of 147 stars. The qualityFlag is a bitmask used to identify issues in *Gaia* astrometry and photometry, with each bit corresponding to a specific quality indicator. We defined our thresholds for these indicators based on the 95$^{\rm th}$ percentile of their cumulative distribution for all sources with G≤13. The specific indicators we flagged are: a re-normalised unit weight error (RUWE) greater than 3.6; an astrometric excess noise greater than 0.61 with a significance greater than 2; and issues related to the integrated pulse duration (IPD), including multi-peak (ipd_frac_multi_peak> 14), harmonic amplitude (ipd_frac_harmonic_amplitude > 0.09), and odd window fraction (ipd_frac_odd_win > 1). Photometric quality flags include a blending fraction (beta) greater than 0.1 and a corrected BP and RP flux excess ($|C^*| > 3\sigma_{C^*}$). Finally, we flagged sources for which specific corrections were applied, as described in Riello et al. (2021) – specifically, the saturation correction (Appendix C.1) and the correction from Sect. 8.4.

Similarly, we considered a subset of 179 M dwarfs from the compilation of Mann et al. (2015). We then established a polynomial relationship between the effective temperature ($T_{\rm eff}$) of the selected stars and their intrinsic *Gaia* DR3 colour $(G_{\rm BP} - G_{\rm RP})_0$. The relationship we obtained is

$$T_{\rm eff} = \sum_{i=0}^{5} c_i (G_{\rm BP} - G_{\rm RP})_0^i, \tag{3}$$

where the best-fit coefficients are reported in Table 3, and the corresponding curve is shown in Fig. 6.

The colour range of validity is $0.43 \leq (G_{\rm BP} - G_{\rm RP})_0 \leq 5$ and the standard deviation of the calibration is 55 K. To be consistent with Casagrande et al. (2010) and following the approach described in Montalto et al. (2021), we initially calculated the effective temperature using Eq. (3) assuming $(G_{\rm BP} - G_{\rm RP})_0 = (G_{\rm BP} - G_{\rm RP})$, i.e. assuming negligible reddening for the adopted stars. We then estimated the monochromatic extinction from Lallement et al. (2022) and converted it to the extinction in all photometric bands. Then we estimated again the intrinsic colour as $(G_{\rm BP} - G_{\rm RP})_0 = (G_{\rm BP} - G_{\rm RP}) - E(G_{\rm BP} - G_{\rm RP})$. We iterated this procedure three times since this was sufficient to obtain convergence on the effective temperature ($\Delta T_{\rm eff} \leq 10$ K).

2.4.2. Radii and masses

Stellar radii for the P4 targets were derived through the empirical relation $Y = a + bX + cX^2$, determined in Mann et al. (2015), where X is the absolute Ks-band magnitude (M_{K_S}) and Y is the stellar radius ($R_\star$). The coefficients a, b, and c of the second-order polynomial fit, taken from Mann et al. (2015), are given in Table 4. This relation is based on the well-established luminosity–radius correlation for main-sequence stars, using absolute Ks magnitudes, M_{K_S}, as a proxy for luminosity. In the case of M dwarfs, this correlation is particularly tight and shows very little dependence on metallicity, making M_{K_S} a reliable predictor of the stellar radius.

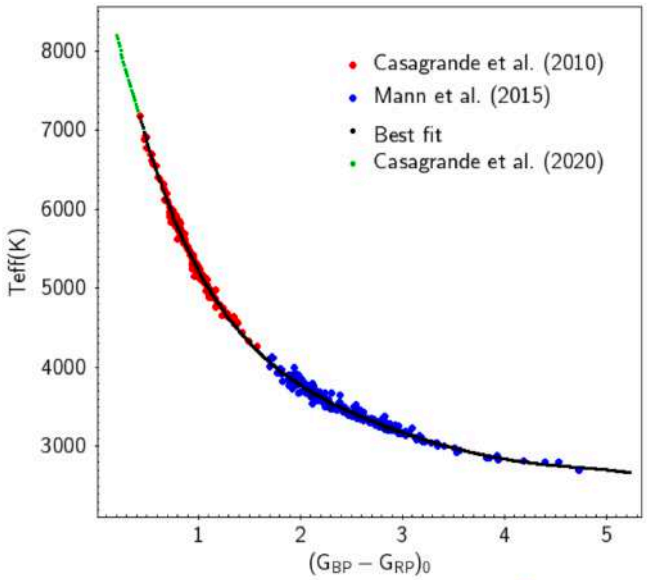

Fig. 6. Best-fit relationship between effective temperature and colour (Eq. (3), black solid line). The red points represent the sample of Casagrande et al. (2010), while the blue points are the sample of Mann et al. (2015). The green line represents Eq. (1) in Casagrande et al. (2021) where we imposed log g=4.438068 and [Fe/H]=0.

Stellar masses for the P4 targets have been derived through the semi-empirical relationship $Y = a + bX + cX^2 + dX^3 + eX^4$, where X is the absolute K-band magnitude (M_{K_S}) and Y is the stellar mass ($M_\star$), also given in Mann et al. (2015). This relation has been constructed using a fourth order polynomial fit between stellar model-derived masses and observed absolute K_S magnitudes, $M_{K_S,0}$, corrected for extinction. The coefficients of such a relation, taken from Mann et al. (2015), are given in Table 4.

The validity range of these relations is $0.1 \lesssim R_*/R_\odot \lesssim 0.7$, corresponding to spectral types K7–M7, with $4.6 < M_{K_S,0} < 9.8$, $2700 < T_{\rm eff} < 4100$ K, and $-0.6 < [{\rm Fe/H}] < 0.5$. These limits are consistent with 97% of the targets in the P4 sample, given that 14 162 out of 14 909 have $M_{K_S,0}$ in this range. The number density of the stellar parameters derived for the P4 sample is shown in Fig. 7.

In order to check the homogeneity of the different methods adopted to derive the stellar radii for the P4 and P5 samples[2], we also show the number density of the subsample of P5 colder than 4500 K. From this comparison, we conclude that the methods adopted to derive stellar radii in the P4 and P5 samples are consistent as the distributions show a smooth continuity, indicating that no systematic discontinuities are introduced by the different methods. Furthermore, we assume that the above relations can be extrapolated for the 474 stars with $3.05 < M_{K_S,0} < 4.6$ that fall outside the validity range, as we observe no discrepancy with the radii derived for the stars with spectral types earlier than M.

[2] The P5 sample includes F5-K7 type stars with $V \leq 13$ (Montalto et al. 2021).

Table 4. Best-fit coefficients from Mann et al. (2015).

Y	X	a	b	c	d	e
R_*	M_{K_S}	1.9515	–0.3520	0.01680	...	...
M_*	M_{K_S}	0.5858	0.3872	–0.1217	0.0106	-2.7262×10^{-4}

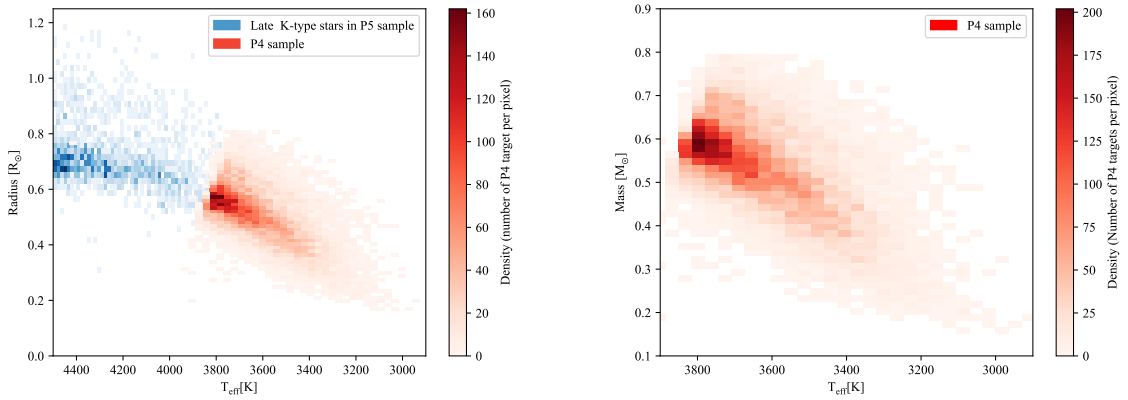

Fig. 7. Distribution of stellar radii (*left*) and masses (*right*) as a function of effective temperature for the P4 sample (red map). The density map in blue corresponds to late-type stars in the P5 sample. The colour intensity indicates the density of stars per bin.

3. Results

3.1. Photometric and volume completeness

Based on the results presented in Gaia Collaboration (2021), we expect the completeness of our sample to be greater than 99% for stars with $V < 16$ (magnitude limit imposed by the science requirement R-SCI-234), as this magnitude limit is well within the range of high completeness for *Gaia* DR3.

To explore the volume completeness of our sample, we used the $\langle V/V_{max}\rangle$ test (Schmidt 1968), originally adopted for quasars. By volume completeness we mean the distance (or volume) within which the P4 sample can be considered statistically complete, i.e. not affected by incompleteness due to observational limits. This approach evaluates whether the distribution of objects in a sample remains statistically uniform within a given maximum radius R_{max}, beyond which incompleteness effects may become significant. In a uniformly distributed sample, $\langle V/V_{max}\rangle$ has a Poisson distribution and its expected value E is 0.5, while the statistical uncertainty is $\sigma = 1/\sqrt{12N}$. This uncertainty derives from the variance $\sigma^2 = 1/12$ of a single variable uniformly distributed between 0 and 1. Therefore, a sample is considered complete if $\langle V/V_{max}\rangle$ is statistically consistent with 0.5 within a defined confidence interval. In particular, compatibility within $\pm3\sigma$ is typically adopted as a robust criterion, assuming purely random (Poisson) statistics.

To apply this test, we selected a subset of stars with absolute magnitudes in the range $7 \leq M_G \leq 14$, which is the magnitude range covered by our targets. For each star i, we defined the volume V_i, enclosed within its observed distance d_i. We then defined a set of increasing values[3] of R_{max} from 0 to 100 pc, in steps of 1 pc. For each R_{max}, we computed the total volume $V_{max} = \frac{4}{3}\pi R^3_{max}$ and selected stars with $d_i \leq R_{max}$. The mean $\langle V/V_{max}\rangle$ value was then computed as $\langle V/V_{max}\rangle = \frac{1}{N}\sum_i \frac{V_i}{V_{max}}$, where N is the number of stars in the sample with distances within R_{max}.

[3] $R_{max} = 100$ pc was chosen because Fig. 2 shows that, beyond this distance, our sample no longer includes late-M stars.

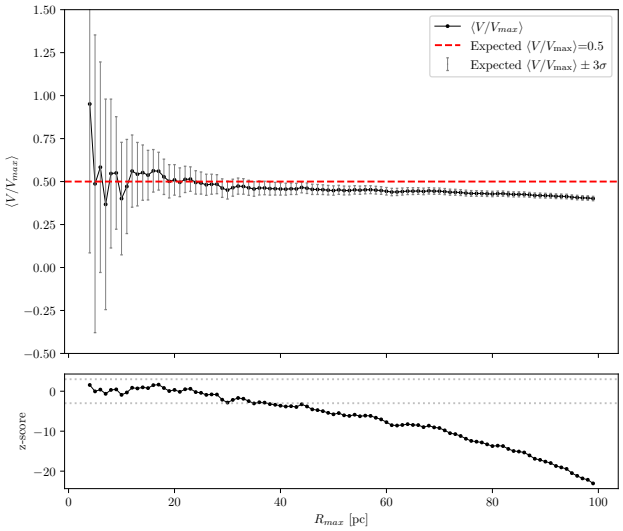

Fig. 8. *Top*: $\langle V/V_{\rm max}\rangle$ as a function of $R_{\rm max}$ for the P4 targets with $7 \leq M_{G,0} \leq 14$, where $V_{\rm max}$ is the corresponding maximum volume. The red dashed line indicates the expected value of 0.5, and the grey error bars show the 3σ statistical uncertainty. *Bottom*: z-score of the deviation from the expected 0.5 value, defined as $z = (\langle V/V_{\rm max}\rangle - 0.5)/\sigma$, as a function of $R_{\rm max}$. The horizontal dotted grey lines indicate the $\pm3\sigma$ limits used to assess the completeness of the sample.

Figure 8 shows $\langle V/V_{max}\rangle$ as a function of R_{max}. The horizontal dashed red line marks the expected value of 0.5 for a homogeneous distribution, while the error bars represent the 3σ confidence interval around this value. In order to establish the distance at which the P4 sample can be considered complete, we computed the deviation from 0.5 normalised by its uncertainty, i.e. the z-score defined as $z = (\langle V/V_{\rm max}\rangle - 0.5)/\sigma$. We found that the distribution remains compatible with 0.5 up to $R_{\rm max} \simeq 37$ pc when considering a 3σ threshold. At larger distances, deviations from the expected value indicate the onset of incompleteness due to the imposed limiting magnitude.

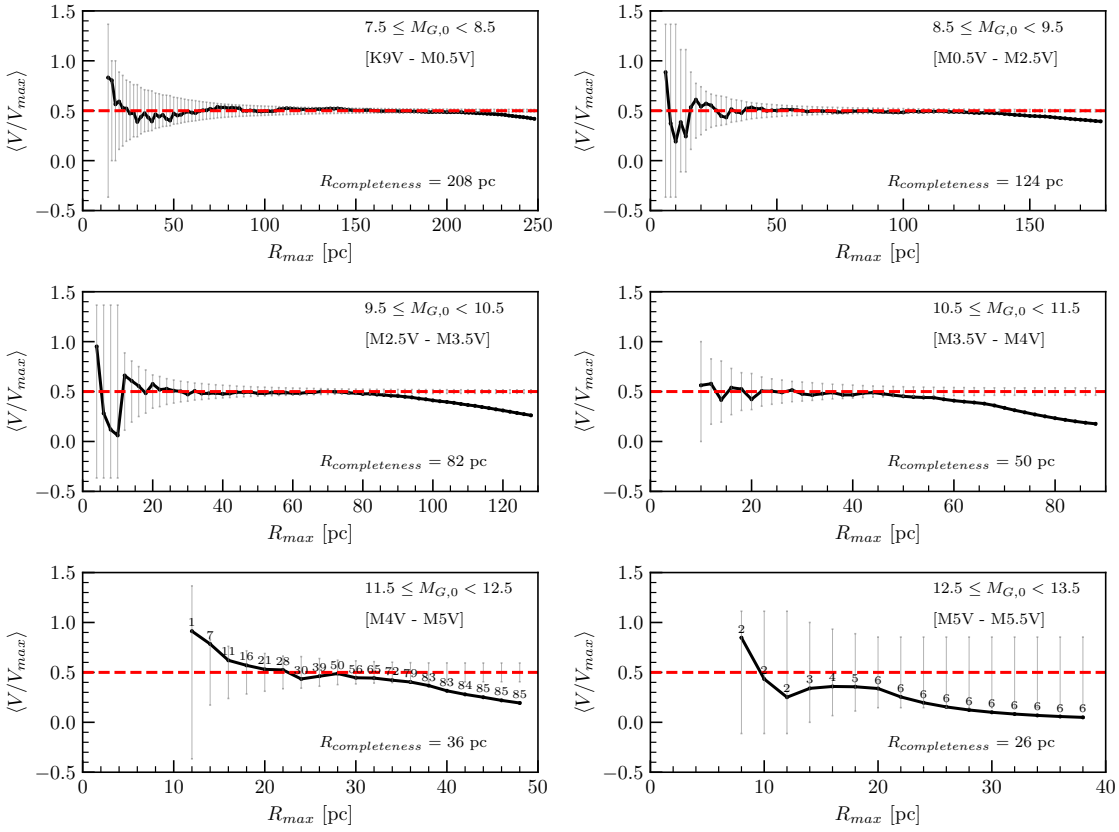

Fig. 9. <V/V_{max}> vs R_{max} corresponding to the volume V_{max} for the P4 sample in different absolute magnitude ranges in the G band. The symbols are as in Fig. 8. The number in each bottom panel indicates the number of stars detected at each distance range.

To evaluate the volume completeness of our sample as a function of spectral type, or, equivalently, of absolute magnitude M_G, we applied the same method described above. Specifically, we computed the $\langle V/V_{\rm max}\rangle$ statistics in successive 1-magnitude-wide bins of M_G, ranging from M_G = 7.5 to M_G = 13.5. These bins were chosen to cover representative ranges of late K and early to mid M-type main-sequence stars. The results are shown in Fig. 9, where we report, for each magnitude bin, the completeness distance ($R_{\rm completeness}$), defined as the distance within which the sample is statistically consistent with a uniform distribution at the 3σ level. For the two magnitude bins in which the samples are more sparsely populated (bottom panels), the number of stars detected in each distance interval is also reported.

These results indicate that the volume completeness of the P4 sample declines towards later spectral types, as the corresponding stars are fainter and detectable only within shorter distances. While the P4 sample includes stars down to spectral type M5V (see Fig. 9), it is overall complete only within a radius of approximately 26 pc, confirming the previous finding from Fig. 8. At larger distances, the number of observed stars increasingly falls short of the number expected from a uniform distribution. In contrast, stars of earlier types, such as M0.5V, remain complete out to 208 pc.

3.2. Galactic spatial-velocity components and P4 stellar population classification

In this section, we present the Galactic space velocities of the P4 targets in order to investigate their kinematic properties and possible membership to different Galactic populations. The resulting classification gives us an indirect estimate of the metallicity of the P4 sample by associating stars with different Galactic populations, which are known to have distinct metallicity distributions.

The Galactic spatial-velocity components (U, V, W) were computed as in Maldonado et al. (in preparation). In particular, these components were derived using *Gaia* DR3 parallaxes, proper motions, and radial velocities, following the method outlined by Montes et al. (2001) and Maldonado et al. (2010). Radial velocities were retrieved from the *Gaia* Archive for 14 625 of the 15 157 stars included in the P4 sample. The uncertainties were calculated by considering the full covariance matrix ensuring that correlations between the astrometric parameters were accounted for.

The uncertainties in the velocity components were computed using the astrometric parameters provided in *Gaia* DR3. Since *Gaia* DR3 does not provide covariance terms for radial velocities, only the astrometric part of the covariance matrix was included in the error propagation. The covariance elements $\mathrm{cov}(\varpi, \mu_{\alpha*})$, $\mathrm{cov}(\varpi, \mu_\delta)$, and $\mathrm{cov}(\mu_{\alpha*}, \mu_\delta)$ were obtained from the corresponding correlation coefficients $\rho(\varpi, \mu_{\alpha*})$, $\rho(\varpi, \mu_\delta)$, and $\rho(\mu_{\alpha*}, \mu_\delta)$, provided by *Gaia* DR3, through the relation

$$\mathrm{cov}(x, y) \propto \rho(x, y)\, \sigma_x\, \sigma_y,$$

where σ_x and σ_y are the uncertainties of the two astrometric parameters. The final uncertainties in (U, V, W) were then derived by propagating both the individual variances and the above covariance terms in quadrature.

The Toomre diagram for the P4 sample, shown in Fig. 10, provides insight into the kinematic classification of the stellar populations (e.g. Fuhrmann 2004). This diagram shows the

Table 5. Comparison of literature radii. Statistical values for fractional residuals, defined as $\frac{R_{\rm lit}-R_{\rm PIC}}{R_{\rm PIC}}$, where $R_{\rm PIC}$ is the PIC2.1.0.1 radius.

Ref.	Mean $\left(\frac{\Delta R}{R_{\rm PIC}}\right)$	$\sigma_{\Delta R}/R_{\rm PIC}$	Median $\left(\frac{\Delta R}{R_{\rm PIC}}\right)$	MAD $\left(\frac{\Delta R}{R_{\rm PIC}}\right)$	N
Gaia DR3 radius_flame	0.112	0.071	0.099	0.035	9909
Morrell & Naylor 2019	0.043	0.047	0.038	0.024	606
Schweitzer+ 2019	–0.027	0.050	–0.030	0.026	291
Mann+15	–0.008	0.053	–0.001	0.030	83

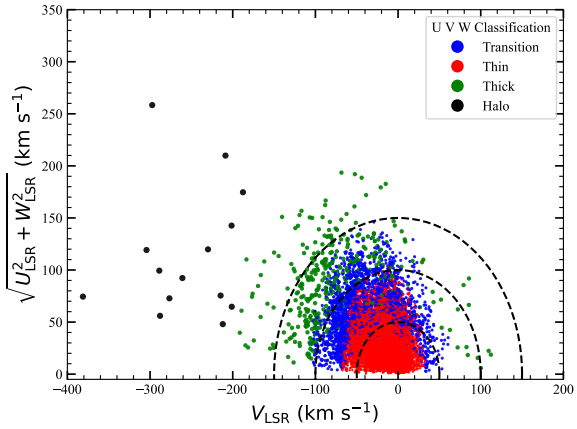

Fig. 10. Toomre diagram for the P4 sample. The different Galactic populations are in distinct colours. The dashed lines indicate constant total velocities, $V_{total} = \sqrt{U_{LSR}^2 + V_{LSR}^2 + W_{LSR}^2}$, for values of 50, 100, and 150 km/s.

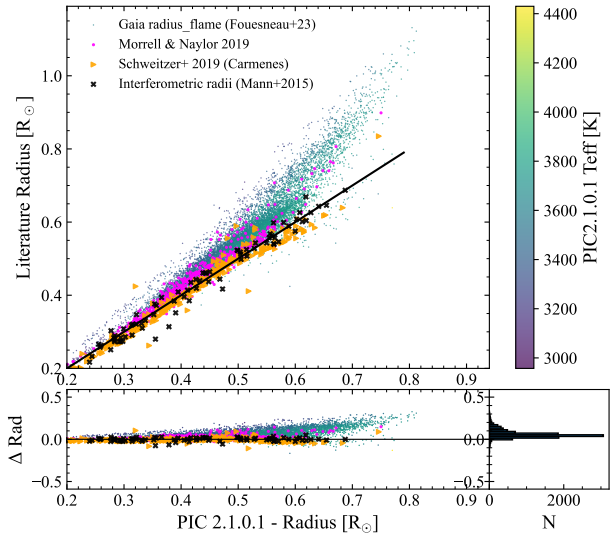

Fig. 11. Comparison of stellar radii from different sources. *Top*: comparison between P4 radii estimated in this work (x-axis) and the `radius_flame` values from *Gaia* DR3 (y-axis), shown with a colour map representing the effective temperature. The radii from other literature works are also shown. The solid line is the 1:1 relation. *Bottom*: distribution of the differences between the P4 radii and *Gaia* DR3 `radius_flame` values and other external literature estimates.

quantity $\sqrt{U_{\rm LSR}^2 + W_{\rm LSR}^2}$, i.e. the combined radial and vertical velocity components orthogonal to the direction of Galactic rotation, as a function of $V_{\rm LSR}$, the tangential velocity component. Here, $U_{\rm LSR}, V_{\rm LSR}, W_{\rm LSR}$ are the heliocentric Cartesian velocity components corrected for the solar motion with respect to the Local Standard of Rest (LSR). The total velocity in the radial and vertical directions reflects how much a star deviates from a circular orbit in the Galactic plane and contributes to its overall kinetic energy.

In order to classify the stars into thin/thick disk populations, we use the approach described by Bensby et al. (2003, 2005). In brief, by assuming that the space velocities for the different Galactic populations have Gaussian distributions, the authors provide equations to calculate the probabilities that a given star belong to the thin disk, the thick disk, or the halo. For each star, the relative probabilities $P_{\rm thick}/P_{\rm thin}$ and $P_{\rm thick}/P_{\rm halo}$ are calculated. Thin disk stars are selected as those with $P_{\rm thick}/P_{\rm thin} < 0.1$, while thick disk stars are those with $P_{\rm thick}/P_{\rm thin} > 10$. Additionally, $P_{\rm thick}/P_{\rm halo} > 1$ is required for both thin and thick disk stars. We find that 11978 stars (81.9%) belong to the thin disk, indicating a population with relatively low velocity dispersion and typical disk-like kinematics. A small fraction of stars (2.63%, 385 in total) are associated with the thick disk, characterised by higher velocity dispersions and older stellar ages. Additionally, 15.36% of the stars (2247 in total) are classified as transition objects, as they occupy an intermediate region between the thin and thick disk populations. These stars may represent a mix of both populations or stars in kinematic transition. Finally, a very small fraction (0.13%, 15 in total) is identified as halo stars, which exhibit high velocities and are likely part of the Galactic halo, a population dominated by older stars on more eccentric orbits. This sample includes the Kapteyn's star (GL 191, Gaia DR3 4810594479418041856) with the components (U, V, W) = (20.07±,0.03, −287.92,±0.10, −52.30±0.07) km s^{-1}, consistent with the values (21.1±0.3, −287.8±0.3, −52.6±0.3) km s^{-1} given in Kotoneva et al. (2005).

4. Discussion

4.1. Stellar radii: Comparison with other studies

Stellar radii included in the P4 sample have been compared with literature values. We first considered the radii of the P4 targets released by *Gaia* DR3 (Fouesneau et al. 2023), taken from the table `gaiadr3.astrophysical_parameters` of the ESA *Gaia* archive, namely `radius_gspphot` and `radius_flame`. The latter were obtained with the Final Luminosity Age Mass Estimator (FLAME, Creevey et al. 2023), designed to determine stellar mass and evolutionary parameters for *Gaia* sources. It is based on the outputs from General Stellar Parametrizer from Photometry (GSP-Phot, Andrae et al. 2023) and General Stellar Parametrizer from Spectroscopy (GSP-Spec, Recio-Blanco et al. 2023), as well as astrometry, photometry, and stellar models, to estimate parameters such as radius, luminosity, gravitational redshift, mass, age, and evolutionary stage.

Results of this comparison are shown in Table 5 and Fig. 11. The comparison reveals a significant discrepancy between the P4 radii and those provided by *Gaia* DR3, considering both

radius_flame and radius_gspphot. In particular, the *Gaia* radii are systematically larger than those estimated for early type M-stars of the P4 sample, reaching values of up to 1 $R_\odot$, which is surprising and unexpected for M-type stars. A better agreement is observed in the comparison with other works, focused on M dwarfs. In particular, we considered radii obtained with two different independent methods, namely the modified SED fitting method proposed by Morrell & Naylor (2019), and the method based on the luminosity from integrated broadband photometry, adopted in Schweitzer et al. (2019). For reference, the comparison with the direct method of the interferometric radii by Mann et al. (2015), used for the calibration adopted in this work, is also indicated.

Table 5 summarises the comparison between the PIC2.1.0.1 stellar radii and values from literature. We report the mean fractional residuals, their standard deviation, the median, the MAD, and the number of stars in common for each dataset. Although the PIC radii show a systematic offset of about 10% compared to *Gaia* DR3 values, they are generally in good agreement with other literature measurements. As expected, for the Mann et al. (2015) sample (the same used to derive the calibration adopted in this work), the median fractional difference is close zero, with a MAD of 0.030, showing a negligible systematic offset and a typical scatter of about 3%. The Morrell & Naylor (2019) radii are slightly larger on average (median residual 0.038), while the Schweitzer et al. (2019) sample shows a small negative offset (median –0.030). In all cases, the scatter is quantified using the median absolute deviation of the fractional residuals, which is lower than 3% (if we do not consider the comparison with *Gaia* DR3), indicating that the PIC radii are consistent with the literature values within a few percent.

As noted above, the Morrell & Naylor (2019) radii are also slightly larger than the radii estimated for the P4 targets. This evidence is in agreement with the conclusions given by Morrell & Naylor (2019) themselves, who stated that the discrepancy with interferometry-anchored methods (such as Mann et al. 2015) can arise from the inclusion of active M dwarfs in the sample. The magnetic activity/starspot effect is known to cause larger radii for active stars compared to their inactive counterparts (Kiman et al. 2024). Furthermore, this effect decreases towards smaller radii (López-Morales 2007; Kiman et al. 2024), and aligns with the trend observed in our comparison.

In order to understand the disagreement with *Gaia* DR3 data, we investigated other *Gaia* astrophysical parameters, namely teff_gspphot and ag_gspphot, from which the radius_flame are derived using the Stefan-Boltzmann law. Figure 12 shows the comparison between the effective temperatures as a function of the extinction values A_G included in the PIC 2.1.0.1 and derived using the Lallement et al. (2022) 3D interstellar extinction map (upper panel) and those provided by *Gaia* DR3 (middle panel). colour symbols represent the Bailer-Jones et al. (2021) distances. The PIC 2.1.0.1 parameters cover the expected range, with very low extinction values that gradually increase with distance. No significant correlation is observed between extinction and effective temperature. On the contrary, we find that the GSP-phot A_G values, i.e. the extinction in the *Gaia* passband predicted by *Gaia* DR3, are unexpectedly large for nearby M-type stars, such as those in the P4 sample, which are located at close distances (<400 pc) from the Sun. In addition, we find that the GSP-phot A_G values are strongly correlated with the GSP-phot $T_{\rm eff}$, in particular for the objects with GSP-phot $A_G \geq 1$. These sources are distributed over a wide range of distances, and their position in the

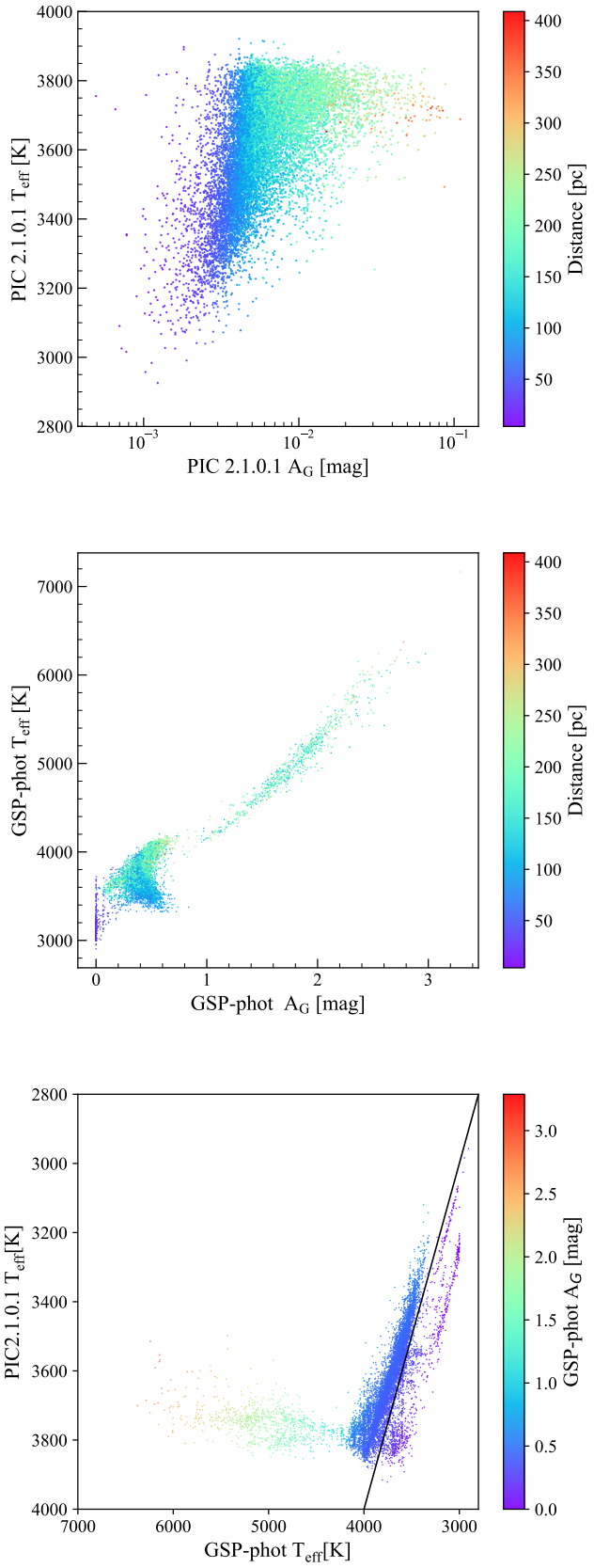

Fig. 12. Effective temperatures and extinction derived in PIC 2.1.0.1 (*top*) and *Gaia* DR3 (*middle*). The colour indicates the *Gaia* DR3 distance. The bottom panel compares GSP-phot (*x*-axis) and PIC 2.1.0.1 (*y*-axis) effective temperatures, colour-coded by GSP-phot extinction. The solid line marks the one-to-one relation.

colour-magnitude diagram deviates from a standard MS as their effective temperatures are higher than expected. We discard the hypothesis that the subgroup with GSP-Phot $A_G > 1$ are actually hotter stars reddened by dust located behind nearby star forming regions, since their spatial distribution across the PLATO field is uniform, similarly to the rest of the sample. The bottom panel of Fig. 12 highlights this behaviour by directly comparing the effective temperatures derived from GSP-phot and PIC 2.1.0.1. A systematic deviation from the one-to-one relation is visible, especially for stars with GSP-phot extinction values $A_G > 1$, for which GSP-phot $T_{\rm eff}$ are significantly overestimated with respect to PIC 2.1.0.1. A consistent fraction of the population shows GSP-phot temperatures in the range $3500 \lesssim T_{\rm eff} \lesssim 4200$ K and moderate extinction ($0.2 \lesssim A_G \lesssim 0.6$), which are significantly higher than those tabulated in the PIC 2.1.0.1. Similar discrepancies in GSP-phot A_G and GSP-phot $T_{\rm eff}$ were already highlighted by Gaia Collaboration (2023a), for stars with $T_{\rm eff} < 4500$ K, in their comparison of high-quality Gaia DR3 astrophysical parameters with reference values from isochrones. A possible reason for this discrepancy is the well-known temperature-extinction degeneracy which has been observed in Gaia DR3 data for cool stars, as discussed in Andrae et al. (2023).

Our results are in agreement with the recent findings of Kiman et al. (2024), who presented a model-independent approach based on the surface brightness-colour relation (SBCR) and Gaia DR3 colours, calibrated using interferometric angular diameters. Kiman et al. (2024) found a clear systematic trend between their results and analogous SBCR radii from Salsi et al. (2021) based on $G - K_S$ colours, for stars with $M < 0.6\,M_\odot$. On the contrary, a good agreement was observed with Mann et al. (2015), on which the calibration for deriving the radii of the P4 sample stars is based.

A detailed comparison by Kiman et al. (2024) of SBCR radii with those derived from Gaia DR3 GSP-Phot and FLAME shows that, for M-type stars (radii < 0.6, $R_\odot$), an offset between 10% and 25% is observed, with Gaia DR3 GSP-Phot and FLAME radii tending to be systematically larger than those inferred from SBCR, depending on the models adopted for the GSP-Phot or FLAME radius estimates. They also show that a comparison between radii derived from direct angular diameter measurements, used for their calibration sample, and GSP-Phot radii reveals a systematic offset of about 10%, with radii derived from direct angular diameter measurements resulting smaller than the *Gaia* GSP-Phot ones.

Based on these considerations, we conclude that the *Gaia* DR3 FLAME and GSP-Phot parameters, including stellar radii, effective temperatures, and A_G, should be used with caution for stars with $T_{\rm eff} < 4200$ K, as evidence of systematic overestimation of these parameters has been found both in our analysis and in previous studies.

4.2. Luminosity spread in low-mass stars: Effects of metallicity and magnetic activity

One of the most intriguing unresolved issues concerning M-type stars in the *Gaia* era is the observed spread in the CAMD. While M-type stars in open clusters generally follow a well-defined sequence, field stars exhibit a broader distribution, as seen in Fig. 2. This spread suggests the presence of additional physical effects influencing the luminosity of M dwarfs beyond the expected evolutionary trends.

A possible explanation for this broadening is the combined effect of metallicity and magnetic activity. Metallicity variations and radius inflation can shift the position of stars in the CAMD

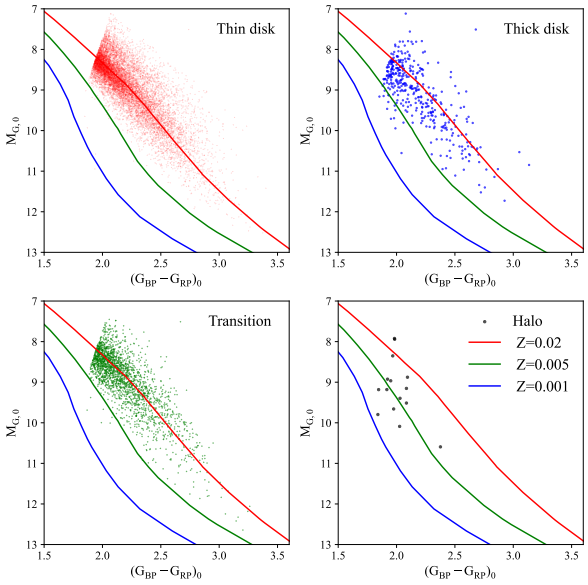

Fig. 13. CAMD of the different P4 galactic populations, compared with 1 Gyr isochrones computed at three different metallicity values (Bressan et al. 2012).

by altering their intrinsic luminosities and colours, as metal-rich stars tend to be redder and fainter for a given mass.

In order to highlight these effects, we considered the classification based on the probability of the stars of being thin, thick, halo or transition stars derived as described in Sect. 3.2. The four samples of targets are shown in Fig. 13. As already noted, the vast majority of P4 targets are thin disk stars, consistent with a relatively young population, while only a small fraction of P4 targets are classified as thick disk and halo stars, consistent with an older population, expected to be more metal-poor than the thin disk stars.

To statistically compare the different Galactic components, we performed the two-sample Kolmogorov-Smirnov (KS) test (Massey 1951) and the Anderson-Darling (AD) test (Anderson & Darling 1952). The KS and AD tests assess whether two samples come from the same underlying distribution, with the AD test being more robust and sensitive to differences in the tails of the distributions.

We applied the KS and AD tests to the effective temperature distributions of stars in the three different Galactic populations: thin disk, thick disk, and halo. The cumulative distributions are shown in Fig. 14, while the results of the tests are given in Table 6. We did not consider the transition sample, since it includes unclassifiable targets.

Since all KS p-values are below the conventional 0.05 threshold, we reject the null hypothesis that the compared samples are drawn from the same parent distribution, in all cases. Similarly, the AD p-values are all ≤0.001, further confirming significant differences in the effective temperature distributions among the Galactic populations. As expected, the largest discrepancy is found between the thin disk and the halo (AD statistic = 15.4), indicating a stronger divergence than that between the thick disk and the halo (AD statistic = 7.1), which is nonetheless also statistically significant. These results support the scenario in which stars from different Galactic components originated from distinct formation and evolutionary processes. Consequently, they suggest that part of the observed spread could be attributed to the inclusion of stars with varying metallicity, as we can see

Table 6. Results of the KS and AD statistical tests for comparisons between the distributions of effective temperature, distance, and apparent V magnitude among the three Galactic populations.

	Populations	KS Stat.	KS p-val.	AD Stat.	AD p-val.
Effective Temperatures	Thin disk vs thick disk	0.1041	5.65×10^{-4}	13.7656	<0.001
	Thick disk vs halo	0.4762	1.60×10^{-3}	7.0925	<0.001
	Thin disk vs halo	0.5536	7.51×10^{-5}	15.4174	<0.001
V Magnitude	Thin disk vs thick disk	0.0439	0.456	−0.3552	0.250
	Thick disk vs halo	0.1273	0.950	−0.5730	0.250
	Thin disk vs halo	0.1376	0.903	−0.2058	0.250
Distance	Thin disk vs thick disk	0.0786	0.0188	3.7200	0.0103
	Thick disk vs halo	0.1939	0.583	0.0062	0.250
	Thin disk vs halo	0.1763	0.677	−0.0946	0.250

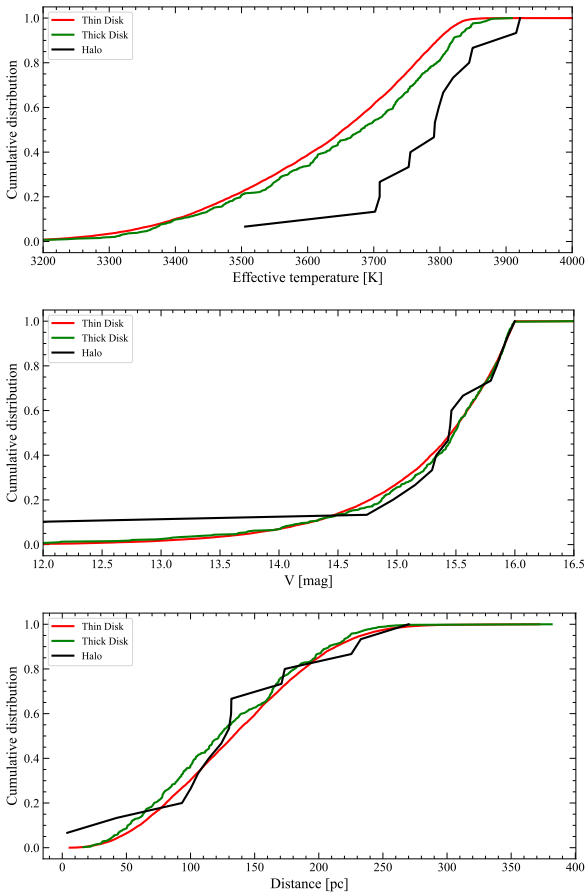

Fig. 14. Cumulative distributions of effective temperature (*top*), V magnitude (*middle*), and distance (*bottom*) of the three different Galactic populations.

in Fig. 13, where PARSEC isochrones at 1 Gyr and different metallicities (Z=0.02, 0.005, 0.001) are overplotted.

The figure highlights how the location of the few halo stars is consistent with the low-metallicity isochrones, while higher-metallicity models are consistent with thin disk stars. The thick disk population, as expected, lies in between, following an intermediate metallicity sequence. This supports the interpretation that the spread in the colour–magnitude distribution is at least partly driven by metallicity differences across the Galactic components.

To rule out the possibility that our results are influenced by selection effects, we also compared the cumulative distributions of the V magnitudes, used in the selection of the P4 sample, and the distances. As shown in Fig. 14, these distributions largely overlap, suggesting that the three Galactic populations share similar characteristics in these parameters.

This visual impression is supported by the KS and AD statistical tests, which quantify the significance of any differences between the distributions. The results, summarised in Table 6, show that for both V magnitude and distance, the p-values are well above the conventional threshold of 0.05, indicating no statistically significant differences. Thus, the distributions are statistically compatible.

The only statistically significant result is the difference between the distance distribution of the thin disk population and that of the thick disk population. However, we consider this fact unlikely to introduce a relevant selection bias in our analysis. We conclude that the observed differences in the effective temperature distributions can be confidently attributed to metallicity.

On the other hand, the magnetic activity, particularly in low-mass stars, can lead to radius inflation and starspot coverage, affecting the observed magnitudes and colours. For example, Somers & Stassun (2017); Jeffries et al. (2021); Franciosini et al. (2022) have shown that starspots can have a significant impact on age determinations. Therefore, these effects should be carefully disentangled to properly interpret the distribution of M dwarfs in the CAMD and to understand the underlying stellar physics at play. To investigate these possible activity effects, we compared in Fig. 15 the position in the CAMD of the stars in the different Galactic populations with a solar metallicity 200 Myr old isochrone, calculated with the Pisa evolutionary code including the effect of starspots (Tognelli et al. 2011; Dell'Omodarme et al. 2012; Tognelli et al. 2015b,a, 2018; Franciosini et al. 2022). This effect is quantified through the parameter

$$\beta = \frac{A_{\rm spotted}}{A_\star}\left(1 - \frac{T^4_{\rm spot}}{T^4_0}\right), \tag{4}$$

which represents the effective spot coverage fraction, accounting for both the ratio between the spotted and unspotted stellar surface temperatures, T_{spot}/T_0 and the actual fraction of the surface covered by spots. The parameter β provides a direct link between the unspotted stellar effective temperature T_0 predicted by stellar models and the observed effective temperature, which is reduced

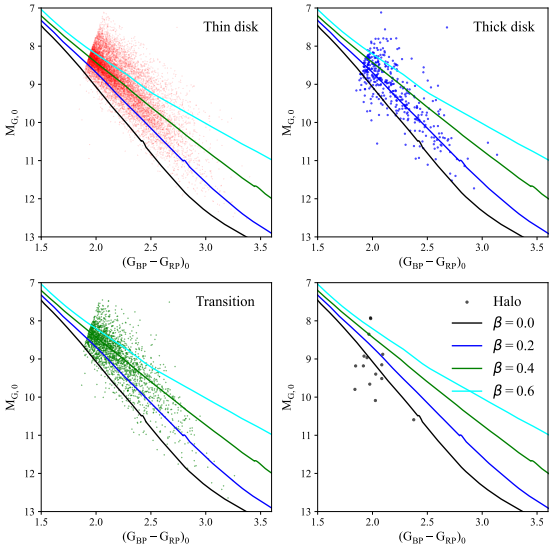

Fig. 15. CAMD of the different P4 galactic populations, compared with a 200 Myr solar metallicity isochrone with different β_{spot} values (Franciosini et al. 2022).

by the presence of spots, according to

$$T_{\rm eff} = T_0\,(1-\beta)^{1/4}. \quad (5)$$

For a given isochrone with age <200 Myr, the inclusion of the starspot effects is parametrised by the four $\beta_{\rm spot}$ = 0.0, 0.2, 0.4 and 0.6 values, with $\beta_{\rm spot}$=0.0 corresponding to unspotted isochrones (see Fig. 15).

Since our samples include stars of any age, such models suffer from the β-age degeneracy that hampers a reliable estimate of stellar ages and simultaneously constrain the most suitable β value. However, the comparison that we present shows that, in case of young stars ($\lesssim$200 Myr), even starspots effects can contribute to the observed spread. In fact, this effect results in a reduced effective temperature that can enhance the spread in the CAMD for a given age.

Additional factors such as unresolved binarity, potential uncertainties in distances, or reddening effects may also contribute to the observed spread, which is not limited to M dwarfs but is also seen in earlier-type stars. Taken together with metallicity and activity, these considerations suggest that the origin of the spread remains complex and yet lacks a conclusive explanation.

5. Conclusions

In this work, we presented the selection, validation process and properties of the P4 sample included in the PLATO Input Catalogue and falling in the LOPS2 field.

The selection criteria for the P4 sample were designed to ensure compliance with PLATO's scientific requirements. The selection process relied on an updated photometric calibration to convert *Gaia* magnitudes into the Johnson-Cousins system, as well as a rigorous definition of magnitude and colour boundaries in the CAMD. A new photometric calibration has been used to derive effective temperatures. The final P4 sample consists of 15 157 targets with a mean distance of 135.4 pc and a distribution extending up to approximately 409 pc. We validated the P4 targets by cross-matching with 2MASS to obtain K_S magnitudes, essential for deriving stellar radii and masses using the Mann et al. (2015) photometric calibration.

The completeness analysis confirms that the P4 sample is nearly complete (> 99%) for stars with $V < 16$, ensuring a reliable selection within the PLATO magnitude range. The $\langle V/V_{\rm max}\rangle$ test confirms that our sample is statistically uniform and volume-complete up to ~26 pc. For larger distances, completeness depends strongly on spectral type: the sample remains complete up to ≃50 pc for stars earlier than M4V, while at ≃200 pc, only the earliest M types (M0V–M1V) are still fully represented. This highlights a progressive decline in completeness with later spectral subtypes and increasing distance.

Our comparison with the literature demonstrates that the radii we estimated for M-type stars are in agreement with those obtained with two independent radius estimation methods, all of which take into account the intrinsic complexity of M stars. In contrast, our radii disagree with those derived from *Gaia* DR3 data, as found in Kiman et al. (2024).

Finally, we conclude that the observed spread in the CAMD may be attributed to both metallicity effects and magnetic activity. To estimate the metallicity effects, we classified the P4 targets in different populations, determined using the Galactic spatial-velocity components (U, V, W). Their distribution in the CAMD suggests that metallicity plays a role in the observed spread, even though it is evident only for the few targets classified as halo stars, which include metal-poor stars. This is expected, given that our sample is dominated by thin disk stars, for which a near-solar metallicity is expected. In addition, the spread is also likely affected by magnetic activity, which leads to a reduction in both effective temperature and luminosity, thereby significantly enhancing the observed dispersion. Other factors, such as unresolved binarity, uncertainties in distances, and reddening, may also contribute, and the overall origin of the spread remains complex and not yet fully understood.

Acknowledgements. This work presents results from the European Space Agency (ESA) space mission PLATO. The PLATO payload, the PLATO Ground Segment and PLATO data processing are joint developments of ESA and the PLATO mission consortium (PMC). Funding for the PMC is provided at national levels, in particular by countries participating in the PLATO Multilateral Agreement (Austria, Belgium, Czech Republic, Denmark, France, Germany, Italy, Netherlands, Portugal, Spain, Sweden, Switzerland, Norway, and United Kingdom) and institutions from Brazil. Members of the PLATO Consortium can be found at https://platomission.com/. The ESA PLATO mission website is https://www.cosmos.esa.int/plato. We thank the teams working for PLATO for all their work. V.N., G.P., M.M., S.B., S.D., V.G., D.N., L.M., I.P., L.P., R.R. acknowledge support from PLATO ASI-INAF agreements no. 2022-28-HH.0. This work has made use of data from the European Space Agency (ESA) mission *Gaia* (https://www.cosmos.esa.int/gaia), processed by the *Gaia* Data Processing and Analysis Consortium (DPAC, https://www.cosmos.esa.int/web/gaia/dpac/consortium). Funding for the DPAC has been provided by national institutions, in particular the institutions participating in the *Gaia* Multilateral Agreement. P.M.M., S.M., G.A., M.F. acknowledge financial support from the ASI-INAF agreement no. 2022-14-HH.0. L.P, J.M., L.A., C..A, and E.F. acknowledge support from the Italian Ministero dell'Università e della Ricerca and the European Union – Next Generation EU through project PRIN 2022 PM4JLH "Know your little neighbours: characterising low-mass stars and planets in the Solar neighbourhood". SC acknowledges financial support from PRIN-MIUR-22: CHRONOS: adjusting the clock(s) to unveil the CHRONO-chemo-dynamical Structure of the Galaxy" (PI: S. Cassisi) funded by the European Union – Next Generation EU, and Theory grant INAF 2023 (PI: S. Cassisi). U.H. acknowledges support from the Swedish National Space Agency (SNSA/Rymdstyrelsen). We would like to thank B. Rojas-Ayala, N. Nardetto, M. Schlecker, D. Stamatelos, and N. Miller for their useful comments and suggestions. We thank the anonymous referee for the careful reading of the manuscript and for the valuable comments and suggestions, which helped improve the clarity and the quality of this work.

References

Alei, E., Claudi, R., Bignamini, A., & Molinaro, M. 2020, Astron. Comput., 31, 100370
Alei, E., Marinoni, S., Bignamini, A., et al. 2025, Astron. Comput., 51, 100936

Anderson, T. W., & Darling, D. A. 1952, Ann. Math. Statist., 23, 193
Andrae, R., Fouesneau, M., Sordo, R., et al. 2023, A&A, 674, A27
Bailer-Jones, C. A. L., Rybizki, J., Fouesneau, M., Demleitner, M., & Andrae, R. 2021, AJ, 161, 147
Bensby, T., Feltzing, S., & Lundström, I. 2003, A&A, 410, 527
Bensby, T., Feltzing, S., Lundström, I., & Ilyin, I. 2005, A&A, 433, 185
Berger, D. H., Gies, D. R., McAlister, H. A., et al. 2006, ApJ, 644, 475
Boyajian, T. S., von Braun, K., van Belle, G., et al. 2012, ApJ, 757, 112
Bressan, A., Marigo, P., Girardi, L., et al. 2012, MNRAS, 427, 127
Casagrande, L., Ramírez, I., Meléndez, J., Bessell, M., & Asplund, M. 2010, A&A, 512, A54
Casagrande, L., Lin, J., Rains, A. D., et al. 2021, MNRAS, 507, 2684
Cassisi, S., & Salaris, M. 2013, Old Stellar Populations: How to Study the Fossil Record of Galaxy Formation
Cassisi, S., & Salaris, M. 2019, A&A, 626, A32
Creevey, O. L., Sordo, R., Pailler, F., et al. 2023, A&A, 674, A26
Dell'Omodarme, M., Valle, G., Degl'Innocenti, S., & Prada Moroni, P. G. 2012, A&A, 540, A26
Dressing, C. D., & Charbonneau, D. 2015, ApJ, 807, 45
Feiden, G. A., & Chaboyer, B. 2013, ApJ, 779, 183
Feiden, G. A., & Chaboyer, B. 2014, ApJ, 789, 53
Fouesneau, M., Frémat, Y., Andrae, R., et al. 2023, A&A, 674, A28
Franciosini, E., Tognelli, E., Degl'Innocenti, S., et al. 2022, A&A, 659, A85
Fuhrmann, K. 2004, Astron. Nachr., 325, 3
Gaia Collaboration (Prusti, T., et al.) 2016, A&A, 595, A1
Gaia Collaboration (Smart, R. L., et al.) 2021, A&A, 649, A6
Gaia Collaboration (Creevey, O. L., et al.) 2023a, A&A, 674, A39
Gaia Collaboration (Vallenari, A., et al.) 2023b, A&A, 674, A1
Girardi, L., Groenewegen, M. A. T., Hatziminaoglou, E., & da Costa, L. 2005, A&A, 436, 895
Irwin, J. M., Quinn, S. N., Berta, Z. K., et al. 2011, ApJ, 742, 123
Jeffries, R. D., Jackson, R. J., Sun, Q., & Deliyannis, C. P. 2021, MNRAS, 500, 1158
Kesseli, A. Y., Muirhead, P. S., Mann, A. W., & Mace, G. 2018, AJ, 155, 225
Kiman, R., Brandt, T. D., Faherty, J. K., & Popinchalk, M. 2024, AJ, 168, 126
Kochukhov, O. 2021, A&A Rev., 29, 1
Kopparapu, R. K., Ramirez, R., Kasting, J. F., et al. 2013, ApJ, 765, 131
Kotoneva, E., Innanen, K., Dawson, P. C., Wood, P. R., & De Robertis, M. M. 2005, A&A, 438, 957
Kratter, K., & Lodato, G. 2016, ARA&A, 54, 271
Lada, C. J. 2006, ApJ, 640, L63
Lallement, R., Capitanio, L., Ruiz-Dern, L., et al. 2018, A&A, 616, A132
Lallement, R., Vergely, J. L., Babusiaux, C., & Cox, N. L. J. 2022, A&A, 661, A147
Lambrechts, M., & Johansen, A. 2012, A&A, 544, A32
López-Morales, M. 2007, ApJ, 660, 732
Lovis, C., Snellen, I., Mouillet, D., et al. 2017, A&A, 599, A16
MacDonald, J., & Mullan, D. J. 2012, MNRAS, 421, 3084
Maldonado, J., Martínez-Arnáiz, R. M., Eiroa, C., Montes, D., & Montesinos, B. 2010, A&A, 521, A12
Maldonado, J., Affer, L., Micela, G., et al. 2015, A&A, 577, A132
Maldonado, J., Micela, G., Baratella, M., et al. 2020, A&A, 644, A68
Mann, A. W., Feiden, G. A., Gaidos, E., Boyajian, T., & von Braun, K. 2015, ApJ, 804, 64
Marrese, P. M., Marinoni, S., Fabrizio, M., & Altavilla, G. 2019, A&A, 621, A144
Massey, F. J. 1951, J. Am. Statist. Assoc., 46, 68
Maxted, P. F. L., Miller, N. J., Hoyer, S., et al. 2022, MNRAS, 513, 6042
Montalto, M., Piotto, G., Marrese, P. M., et al. 2021, A&A, 653, A98
Montes, D., López-Santiago, J., Gálvez, M. C., et al. 2001, MNRAS, 328, 45
Morrell, S., & Naylor, T. 2019, MNRAS, 489, 2615
Nascimbeni, V., Bedin, L. R., Piotto, G., De Marchi, F., & Rich, R. M. 2012, A&A, 541, A144
Nascimbeni, V., Piotto, G., Börner, A., et al. 2022, A&A, 658, A31
Nascimbeni, V., Piotto, G., Cabrera, J., et al. 2025, A&A, 694, A313
Olander, T., Gent, M. R., Heiter, U., et al. 2025, A&A, 696, A62
Pecaut, M. J., & Mamajek, E. E. 2013, ApJS, 208, 9
Rauer, H., Aerts, C., Cabrera, J., et al. 2025, Exp. Astron., 59, 26
Rauer, H., Catala, C., Aerts, C., et al. 2014, Exp. Astron., 38, 249
Recio-Blanco, A., de Laverny, P., Palicio, P. A., et al. 2023, A&A, 674, A29
Riello, M., De Angeli, F., Evans, D. W., et al. 2021, A&A, 649, A3
Salsi, A., Nardetto, N., Mourard, D., et al. 2021, A&A, 652, A26
Schlecker, M., Apai, D., Lichtenberg, T., et al. 2024, Planet. Sci. J., 5, 3
Schmidt, M. 1968, ApJ, 151, 393
Schweitzer, A., Passegger, V. M., Cifuentes, C., et al. 2019, A&A, 625, A68
Skrutskie, M. F., Cutri, R. M., Stiening, R., et al. 2006, AJ, 131, 1163
Somers, G., & Stassun, K. G. 2017, AJ, 153, 101
Spruit, H. C. 1982, A&A, 108, 348
Spruit, H. C., & Weiss, A. 1986, A&A, 166, 167
Swayne, M. I., Maxted, P. F. L., Triaud, A. H. M. J., et al. 2024, MNRAS, 528, 5703
Tognelli, E., Prada Moroni, P. G., & Degl'Innocenti, S. 2011, A&A, 533, A109
Tognelli, E., Prada Moroni, P. G., & Degl'Innocenti, S. 2015a, MNRAS, 454, 4037
Tognelli, E., Prada Moroni, P. G., & Degl'Innocenti, S. 2015b, MNRAS, 449, 3741
Tognelli, E., Prada Moroni, P. G., & Degl'Innocenti, S. 2018, MNRAS, 476, 27
Torres, G. 2007, ApJ, 671, L65
Wanderley, F., Cunha, K., Kochukhov, O., et al. 2024, ApJ, 971, 112

[1] INAF-Osservatorio Astronomico di Palermo, Piazza del Parlamento 1, 90134, Palermo, Italy
[2] INAF – Osservatorio Astrofisico di Catania, Via S. Sofia 78, 95123 Catania, Italy
[3] Dipartimento di Fisica e Astronomia "Galileo Galilei", Università degli Studi di Padova, Vicolo dell'Osservatorio 3, 35122 Padova, Italy
[4] INAF – Osservatorio Astronomico di Padova, vicolo dell'Osservatorio 5, 35122 Padova, Italy
[5] INAF – Osservatorio Astronomico di Roma, Via Frascati, 33, 00078 Monte Porzio Catone (RM), Italy
[6] SSDC-ASI, Via del Politecnico, snc, 00133 Roma, Italy
[7] Centro di Ateneo di Studi e Attività Spaziali "Giuseppe Colombo", Università degli Studi di Padova, Via Venezia 1, 35131 Padova, Italy
[8] Deutsches Zentrum für Luft- und Raumfahrt (DLR), Institut für Planetenforschung, Rutherfordstraße 2, 12489 Berlin-Adlershof, Germany
[9] LESIA, CNRS UMR 8109, Université Pierre et Marie Curie, Université Denis Diderot, Observatoire de Paris, 92195 Meudon, France
[10] Aix-Marseille Université, CNRS, CNES, Laboratoire d'Astrophysique de Marseille, Technopôle de Marseille-Etoile, 38, rue Frédéric Joliot-Curie, 13388 Marseille cedex 13, France
[11] Max-Planck-Institut für Sonnensystemforschung, Justus-von-Liebig-Weg 3, 37077 Göttingen, Germany
[12] Department of Physics, University of Warwick, Gibbet Hill Road, Coventry CV4 7AL, UK
[13] Institute of Geological Sciences, Freie Universität Berlin, Malteserstraße 74-100, 12249 Berlin, Germany
[14] Observatoire de Genève, Université de Genève, Chemin Pegasi 51, 1290 Sauverny, Switzerland
[15] Dip. di Fisica e Chimica, Università di Palermo, Piazza del Parlamento 1, 90134 Palermo, Italy
[16] INAF-Osservatorio Astronomico d'Abruzzo, via M. Maggini, sn. 64100, Teramo, Italy
[17] Dipartimento di Matematica e Fisica, Università Roma Tre, Via della Vasca Navale 84, 00146 Roma, Italy
[18] Observational Astrophysics, Department of Physics and Astronomy, Uppsala University, Box 516, SE-751 20 Uppsala, Sweden
[19] INAF-Osservatorio Astrofisico di Torino, via Osservatorio 20, 10025 Pino Torinese, Italy